Progress in Oceanography 79 (2008) 106–119

Contents lists available at ScienceDirect

Progress in Oceanography

journal homepage: www.elsevier.com/locate/pocean

Mesoscale eddies off Peru in altimeter records: Identification algorithms and eddy spatio-temporal patterns

Alexis Chaigneau [a,b,*], Arnaud Gizolme [a,b], Carmen Grados [b]

[a] Institut de Recherche pour le Développement (IRD), Laboratoire d'Océanographie et de Climatologie: Expérimentation et Analyse Numérique (LOCEAN), UMR CNRS, Université P. et M. Curie, IRD, MNHN, Paris, France
[b] Instituto del MAR del PEru (IMARPE), Esquina general Gamarra y Valle, Callao, Peru

ARTICLE INFO

Article history:
Accepted 14 October 2008
Available online 21 October 2008

Keywords:
Mesoscale activity
Eddy identification algorithms
Eddy characteristics
Eddy life cycles
Spatio-temporal variability
Eastern South-Pacific
Humboldt current systems

ABSTRACT

Relatively little is known about coherent vortices in the eastern South-Pacific along the Peruvian coast, even with regard to basic facts about their frequency of occurrence, longevity and structure. This study addresses these issues with nearly 15 years of relatively high-resolution satellite altimetry measurements.

We first compare two distinct automated methods for eddy identification. The objective validation protocol shows that the rarely-used geometrical or "*winding-angle method*", based on the curvature of the streamline functions, is more accurate than the commonly-used "*Okubo–Weiss algorithm*", which defines a vortex as a simple connected region with values of Okubo–Weiss parameter weaker than a given threshold.

We then investigate vortices off Peru using more than 20,000 mesoscale eddies identified by the winding-angle method. Coherent eddies, characterized by a high ratio of vorticity to deformation rate, are typically formed along the coast and propagate westward at 3–6 cm s^{-1}. The vortices have a mean radius of 80 km, increasing northward, and are most frequently observed off of Chimbote (9°S) and south of San Juan (15°S). The mean eddy lifetime is about 1 month, but if eddies survive at least 2 months, the probability for surviving an additional week (or month) is constant at 90% (or 67%). Anticyclonic eddies tend to propagate northwestward whereas cyclonic vortices migrate southwestward. In general, cyclones and anticyclones are similar, except for eddies surviving at least 6 months. In this case, after a similar 3–4 months of radius and amplitude growth, amplitudes (or sizes) decay particularly rapidly for anticyclonic (or cyclonic) eddies. In terms of intensity, cyclonic eddies show a rapid decay during the first 3 months before arriving at a quasi-constant value, whereas anticyclones exhibit steady decline. Finally, eddy temporal variations were examined at seasonal and interannual scales in the "coastal" region favorable to the formation of energetic mesoscale structures. On seasonal scales, eddy activity is maximal in fall and minimum in spring. At interannual scales, the eddy activity index was maximal during the strong El Niño of 1997–1998 but another strong maximum of eddy activity also occurred late in 2004. These temporal variations are probably associated with the intensification of the upwelling thermal front and with the passage of coastal-trapped waves which generate baroclinic instabilities. Further investigation of the mechanisms involved on the eddy genesis is needed.

1. Introduction

The eastern South-Pacific Ocean (ESP), as the World Ocean in general, is a turbulent system which exhibits, superimposed on the large-scale Peru–Chile Current System (Strub et al., 1998), mesoscale variability composed of eddies or vortices (Hormazabal et al., 2004; Chaigneau and Pizarro, 2005c), meanders or fronts (Chaigneau and Pizarro, 2005a), and squirts and filaments (Thomas, 1999). Compared to other ocean basins, the ESP is characterized by relatively low levels of eddy kinetic energy (EKE) (Stammer, 1997, 1998; Stammer and Wunsch, 1999; Le Traon and Morrow, 2001; Stammer et al., 2006; Pascual et al., 2006), varying from 200–300 cm^2 s^{-2} along the continental coast to 50–100 cm^2 s^{-2} in the interior ocean (Hormazabal et al., 2004; Chaigneau and Pizarro, 2005b). Long-lived energetic eddies, having a lifetime higher than 3 months, can nevertheless be generated near the coast and propagate long distances offshore (Chaigneau and Pizarro, 2005c).

Eddies are generally more energetic than the surrounding currents and are an important component of dynamical oceanography at all scales. In particular they can transport heat, mass, momentum, and biogeochemical properties from their regions of forma-

* Corresponding author. Address: Instituto del MAR del PEru (IMARPE), Esquina general Gamarra y Valle, Callao, Peru. Tel.: +51 1 429 60 69/76 30 (anexo 265).
E-mail address: alexis.chaigneau@ird.fr (A. Chaigneau).

0079-6611/$ - see front matter © 2008 Elsevier Ltd. All rights reserved.
doi:10.1016/j.pocean.2008.10.013

tion to remote areas where they can then impact budgets of the tracers (Bryan, 1996; Wunsch, 1999; Roemmich and Gilson, 2001; Jayne and Marotzke, 2002; Qiu and Chen, 2005). In the ESP, the offshore propagation of mesoscale structures can extend the area of high primary productivity (Thomas et al., 1994; Chavez, 1995; Loubere, 2000) through advection of phytoplankton biomass and nutrient-enriched coastal water. It is also hypothesized that the variability of the highly pronounced subsurface oxygen minimum zone observed in the Peru–Chile Current System (Helly and Levin, 2004) is modulated by the westward motions of mesoscale eddies. In the vertical, eddy pumping may be an important mechanism for bringing nutrient-enriched subsurface water into the euphotic zone as observed in other areas of the world ocean (Falkowski et al., 1991; McGillicuddy et al., 1998; Siegel et al., 1999). Finally, mesoscale processes impact marine ecosystems (Logerwell and Smith, 2001; Spear et al., 2001; Bakun, 2006; Sasai et al., 2006) and the management of various marine activities such as fisheries, pollution monitoring, or offshore industry.

Despite the importance of the mesoscale dynamics, only a few works have investigated eddy characteristics of the ESP and none of them have focused on the Peruvian oceanic region which is one of the most productive of the world. Recently, Chaigneau and Pizarro (2005c) used near-surface drifters and satellite altimetry to provide the mean Chile–Peru Current eddy characteristics in a region south of 10°S, but basic questions remain. In particular, mean eddy properties such as geographical distribution, frequency of occurrence, lifespan, and propagation velocity field are all undescribed. Growth and decay of long-lived eddies and the temporal variations of eddy activity and characteristics are also poorly documented. Over the last two decades, satellite altimetry, due to its global and regular monitoring with relatively high resolution, has given considerable insight into mesoscale dynamics. The aim of this study is to use nearly 15 years of altimetry to quantitatively investigate the mesoscale activity and examine its spatio-temporal variability in a region offshore from Peru. The results should be useful for the validation of regional oceanic model simulations, and also to better examine relationships between mesoscale dynamics and marine ecosystems.

Mesoscale vortices cannot be identified and extracted from geophysical turbulent flow as observed by satellite altimetry without suitable definition and a competitive identification algorithm. A multitude of different techniques for automatic identification of eddies have been proposed, based either on physical or geometric criteria of the flow field. Physical criteria require the calculation of dynamical properties, and eddies are identified where thresholds of calculated properties are exceeded. Dynamical properties of the flow field that have been used to identify eddies include pressure or sea-level anomaly magnitude (Jeong and Hussain, 1995; Fang and Morrow, 2003; Morrow et al., 2004a; Chaigneau and Pizarro, 2005c), high vorticity magnitude (Hussain and Huyakawa, 1987), or high normalized helicity (Buning, 1989; Sadarjoen et al., 1998). Other physical criteria based in particular on the velocity gradient tensor or rate-of-deformation tensor have also been used to study coherent oceanic structures (Isern-Fontanet et al., 2003, 2004, 2006; Morrow et al., 2004b; Chelton et al., 2007). However, as mentioned by Sadarjoen (1999), these physical criteria often fail to locate vortices and eddy identification may be inaccurate (Basdevant and Philipovitch, 1994). Furthermore, arbitrarily varying thresholds may need to be used for these methods, requiring a user interaction which leads to a non-fully automated and subjective process.

A second type of eddy identification techniques is based on geometry of the flow. As vortices consist of quasi-circular flow patterns, geometric criteria use the shape or curvature of instantaneous streamlines. These vortex-identification methods consist to release a large number of streamlines over the velocity field of the study domain and select the curves having circular or closed geometry. To this end, two different techniques can be used: (1) the "*curvature center method*" (Leeuw and Post, 1995) or (2) the "*winding-angle method*" (Sadarjoen and Post, 2000), which detects closed streamlines via measuring cumulative changes in streamline direction as represented by the winding-angle (see Appendix). As noted by Sadarjoen (1999) and Guo (2004), these geometrical methods and in particular the winding-angle method, look promising to detect weak vortices.

The first goal of this study is to compare physical and geometrical vortex-identification methods. After having established the suitability of the geometrical method to extract eddies from sea-level anomaly (SLA) maps, we apply this rather rarely-used algorithm to investigate eddy activity off Peru. The paper is organized as follows. Under Section 2, we describe the satellite data set and computation of the different eddy kinematics. Vortex censuses, which involve objective identification and tracking algorithms, are also described in Section 2. In Section 3 we compare both of the eddy detection schemes using an objective protocol of validation. Section 4 deals with the main eddy properties of the study region whereas Section 5 focuses on the genesis, the propagation and the growth and decay of long-lived eddies. The temporal variations of eddy characteristics and eddy activity are investigated in Section 6. A summary of the results is provided in Section 7, along with ideas for future research.

2. Data and methods

2.1. Altimetry data and inferred eddy kinematic properties

Combining data from different satellite missions improves the estimation of mesoscale signals (Le Traon and Dibarboure, 1999; Le Traon et al., 2001; Chelton and Schlax, 2003; Pascual et al., 2006). The altimeter data used in this study are the combined Topex/Poseidon (T/P), ERS-1/2, Jason-1 and Envisat product as provided by Collecte Localisation Satellite (CLS) – Space of Oceanography Division of Toulouse, France. This AVISO delayed-time altimeter dataset provides a homogeneous, inter-calibrated and highly accurate long time-series of SLA data spanning roughly 14 years from October 1992 to August 2006 (datasource: http://www.jason.oceanobs.com).

As explained by Ducet et al. (2000), SLA alongtrack measurements are first filtered with a Lanczos filter having a typical cutoff wavelength of 200–300 km in the study region. These filtered data are then subsampled every 35–50 km and mapped through an objective technique used to combine the distinct satellite alongtrack measurements. This method takes into account long wavelength error uncorrelated noise due to residual orbit errors but also tidal or inverse barometer errors, and high frequency ocean signals (Le Traon et al., 1998). Finally, the merged-satellite product results in 723 weekly SLA maps which are computed relative to a seven year mean (January 1993–December 1999) and distributed on a regular $0.25^\circ \times 0.25^\circ$ grid.

During the ERS-1 ice-monitoring and geodetic mission (26 December 1993–31 March 1995), there were no ERS data available for ocean mesoscale studies. For this period, T/P data alone were used in the merged product and the spatial and temporal decorrelation scales lead to a reduction in EKE levels of around 30% globally (Ducet et al., 2000). Since our study region (3°S–20°S; 70°W–90°W, see Fig. 1) extends near the equator where the T/P groundtrack coverage is coarse (200–300 km), we can expect some reduction in EKE and in the number of identified eddies during the period with only T/P data. We will return to this point during the discussion on the temporal evolution of eddy characteristics in Section 6.

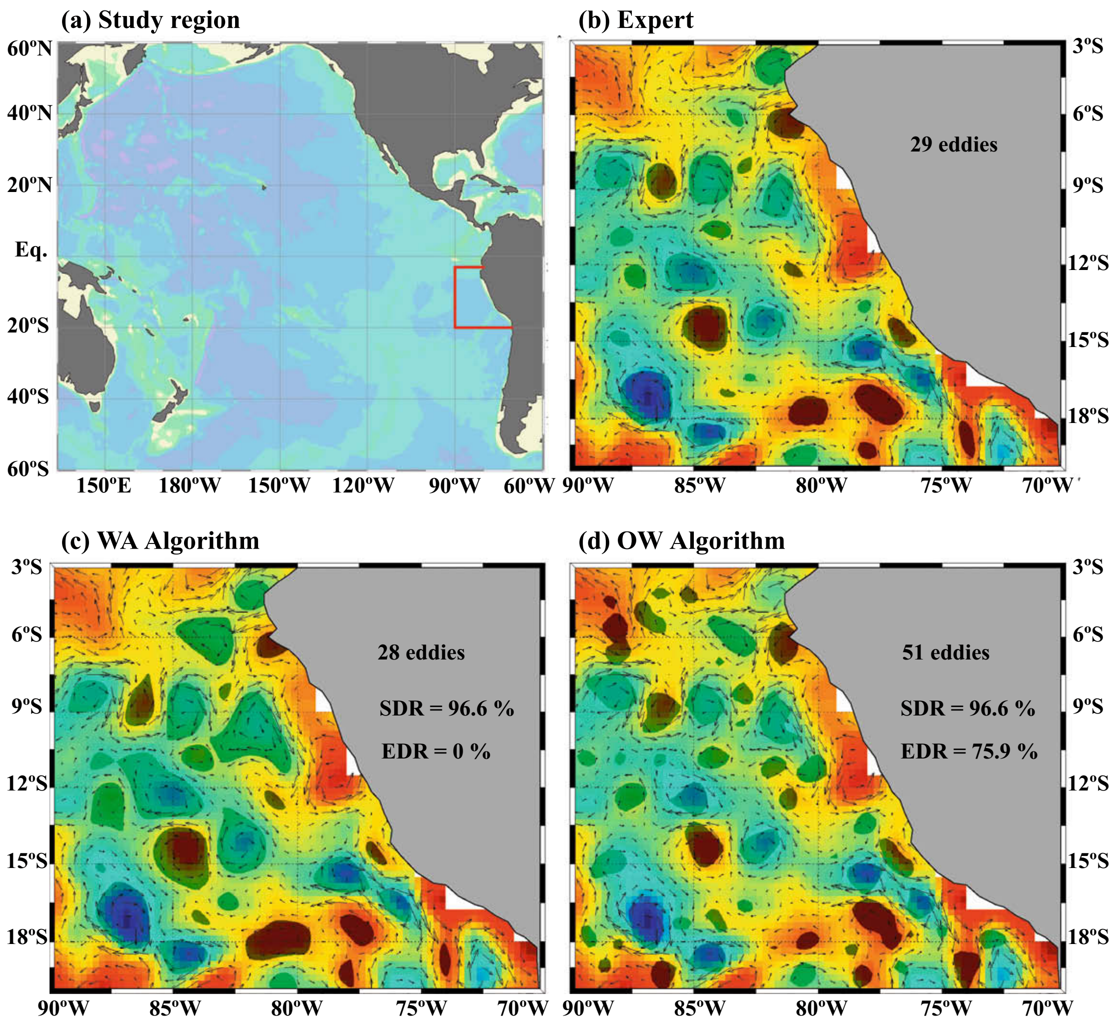

Fig. 1. (a) Study region (red box) and illustrative example for the detection of vortices by (b) one of the experts, (c) the "*winding-angle method*" and (d) the "*Okubo–Weiss method*". Shown are the SLAs (colour shading), the associated geostrophic currents (black quivers) and the identified eddies (light shading). Clockwise rotating structures correspond to cyclonic eddies in the southern hemisphere. The numbers of identified eddies and success and excess detection rates are also indicated.

Considering only the balance between the Coriolis force and the pressure gradient, residual sea-surface geostrophic velocity components (U', V') can be computed from the SLA gradients as

$$U' = -\frac{g}{f}\frac{\partial(SLA)}{\partial y},$$
$$V' = \frac{g}{f}\frac{\partial(SLA)}{\partial x},$$

where g is the acceleration due to gravity, f is the Coriolis parameter, and ∂x and ∂y are the eastward and northward distances. The swirl velocity V_θ of each detected eddy (see Section 3.2) corresponds to the geostrophic velocity amplitude ($V_\theta = \sqrt{U'^2 + V'^2}$).

It is important to note that f tends to zero near the equator and the geostrophic approximation will not be valid north of ~5°S. Consequently, north of 5°S we followed Lagerloef et al. (1999) to compute velocity components on a β-plane; this did not affect significantly the statistical results of this study. We thus assumed that the geostrophic approximation can be applied in the entire study region between 3°S and 20°S and the velocity fields were computed from the definitions given above. Also, the geostrophic approximation for deriving eddy velocities is valid only if centrifugal force and friction are neglected. The comparison of the relative and planetary vorticities (ξ and f, respectively) in the ESP shows that the vorticity rate ($|\frac{\xi}{f}|$), equivalent to the Rossby number, increases when eddy radius decreases (Chaigneau and Pizarro, 2005c): at a radius of 100 km the relative vorticity is about 1% of f and at a radius of 10 km the rate increases to 10%. Since the results of this study are only based on vortices having a radius larger than 35 km (see Section 4.1) which correspond to vorticity rates smaller than 5%, we argue that ageostrophic processes can be neglected.

EKE is computed from velocity components using the classical relation

$$\text{EKE} = \frac{1}{2}(U'^2 + V'^2).$$

To investigate the principal eddy characteristics of the study region we also compute their vorticity and deformation rates. First, in the local Cartesian (x, y) coordinate system, the gradients of geostrophic components are

$$g_{11} = \frac{\partial U'}{\partial x}; \quad g_{12} = \frac{\partial U'}{\partial y}; \quad g_{21} = \frac{\partial V'}{\partial x}; \quad g_{22} = \frac{\partial V'}{\partial y}.$$

Within a 7-day period, it is assumed that g_{11}, g_{12}, g_{21} and g_{22} are constants with respect to location and time. Using these gradients, we can determine the vorticity by

$$\omega = g_{21} - g_{12},$$

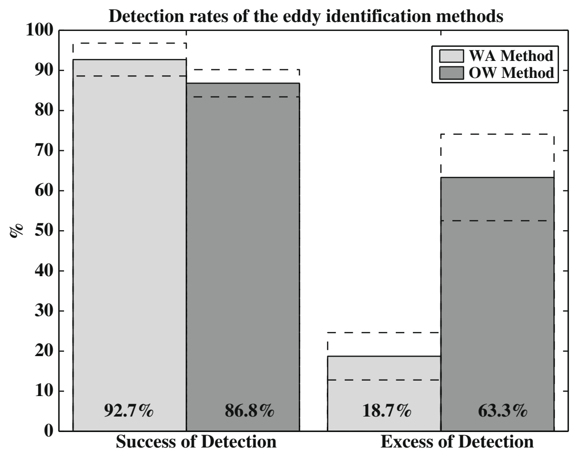

Fig. 2. Detection rates of both the *winding-angle* and *Okubo–Weiss* eddy identification methods. The gray-shading bars and black numbers correspond to the mean values and the means ± one standard deviation are displayed by dashed lines.

the shearing deformation rate (or the shear component of strain) by

$$s_s = g_{21} + g_{12},$$

the stretching deformation rate (or the normal component of strain) by

$$s_n = g_{11} - g_{22},$$

the total deformation rate by

$$s = \sqrt{s_s^2 + s_n^2}$$

and the divergence by

$$\psi = g_{11} + g_{22}.$$

By definition, in the southern hemisphere the vorticity is positive for an anticyclonic (warm-core, or high-pressure) eddy, and is negative for a cyclonic (cold-core, or low-pressure) eddy.

2.2. Eddy identification algorithms and eddy property determination

One of the aims of this study is to compare and quantify the efficiency of two automated methods for eddy identification. The first is based on geometric criteria and was motivated by the following concrete definition of a vortex provided by Robinson (1991):

> *"A vortex exists when instantaneous streamlines mapped onto a plane normal to the vortex core exhibit a roughly circular or spiral pattern (...)"*

This definition suggests the use of streamline function curvatures for the detection of mesoscale eddies and is achieved using the winding-angle (WA) detection algorithm (Sadarjoen et al., 1998; Sadarjoen and Post, 2000; Sadarjoen, 1999; Guo, 2004). This method (hereinafter referred as "*WA method*") characterizes an eddy structure by a point that defines its center and by a closed streamline contour corresponding to the eddy edge. The inner points bordered by this contour line belong to the eddy and determine its surface area. For each SLA map, possible cyclonic (or anticyclonic) eddy centers are identified finding local SLA minima (or maxima) in an arbitrary chosen $1.25^\circ \times 1.25^\circ$ latitude–longitude moving window. Then, streamlines are computed, following the trajectories of virtual particles released in the geostrophic current field from every $0.25^\circ \times 0.25^\circ$ grid point. The step size and the number of steps for the integration of the streamlines must be chosen carefully. The step size should be chosen as small as possible to achieve the highest accuracy while the number of steps should be as high as possible to ensure that paths are long enough, particularly in regions of low velocity magnitude. Here, each streamline is constructed using arbitrary chosen values of 1200 vertices with a constant step size of 0.05 (one twentieth of a cell grid corresponding approximately to 1.35 km). The maximum streamline length is thus of order of 1600 km corresponding to a maximum detectable eddy radius of ~250 km. This value is larger than both the estimated size of the visually identified eddies and the larger Rossby radius of deformation of 225 km observed in the study region (Chelton et al., 1998; see also Fig. 3b).

Then, the eddy identification process consists of two main stages: the *selection* of streamlines associated with eddies and the *clustering* of distinct streamlines corresponding to the same vortex. In the first stage, *selection*, streamlines having a high winding-angle $|\alpha| \geq 2\pi$ (see Appendix for definition of α), corresponding to a fully closed curve, are associated with an eddy center. In the second stage, *clustering*, the streamlines belonging to a given eddy are grouped. Thus, each cluster consists of closed streamlines rotating around the same vortex center. For each cluster, the outer streamline corresponds to the eddy edge. As noted by Isern-fontanet et al. (2003), when a vortex is embedded in background flow, the total streamfunction field does not necessarily exhibit a clear extreme at the eddy center. Consequently, the contours obtained with the WA in the SLA fields are not always associated with closed contours in the total streamfunction field. However, the main statistics obtained from SLA maps and discussed in this paper were also computed from the total streamfunction field adding the barotropic currents of the Rio05 combined mean dynamic topography (Rio and Hernandez, 2004; Rio et al., 2007) produced by CLS Space Oceanography Division (not shown). As no significant differences were observed and as we are interested in eddy dynamics without the influence of large-scale currents, we preferred using the streamfunctions computed from the SLAs.

While WA method is based on geometrical criteria, the second eddy identification method examined is based on a physical criterion. It detects vortices using the properties of the Okubo–Weiss parameter (Okubo, 1970; Weiss, 1991) which indexes the relative importance of strain and vorticity in the flow as

$$W = s_s^2 + s_n^2 - \omega^2,$$

where s_s, s_n and ω are, respectively, the shearing deformation rate, the straining deformation rate and the vorticity defined in Section 2.1.

As suggested in previous marine studies (Isern-Fontanet et al., 2003, 2006; Morrow et al., 2004b; Chelton et al., 2007), a vortex exists where rotation dominates, corresponding to negative W values. More precisely, a vortex is defined as a region having the same sign of vorticity and with values of the OW parameter smaller in magnitude than a threshold $W_0 = -0.2\sigma_w$, σ_w being the spatial standard deviation of W. The geostrophic velocity fields derived from SLA maps are used to compute σ_w at each time, and closed contours of $W = W_0$ are assigned to eddies. This second vortex-identification algorithm is hereinafter referred as "*OW method*".

The two eddy identification algorithms described above are applied to the entire altimetry dataset to detect eddy edges in the study region. After a vortex edge is identified, several eddy properties are computed. The position of the vortex center is determined as the position of the maximum absolute value of SLA inside the eddy. The vortex area (A) corresponds to the area delimited by eddy edge whereas its apparent radius (R) corresponds to the radius of an equivalent circular vortex having the same area

$$R = \sqrt{\frac{A}{\pi}}.$$

By analogy with atmospheric studies of cyclone activity (e.g. Nielsen and Dole, 1992; Zhang et al., 2004; Wang et al, 2006), we define the vortex amplitude as the absolute value of the SLA difference between the eddy center and the averaged SLA along the eddy edge:

$$\text{Amplitude} = |SLA_{center} - \overline{SLA_{edge}}|.$$

Eddy intensity (EI), or energy density, corresponds to the mean EKE over the vortex ($\overline{\text{EKE}}$) normalized by its area

$$\text{EI} = \frac{\overline{\text{EKE}}}{A} = \frac{\overline{\text{EKE}}}{\pi R^2}.$$

Finally, to measure the overall eddy activity in the study region, we use an eddy activity index (EAI) that is defined as

$$\text{EAI} = N\overline{\text{EI}} = \sum_{i=1}^{N} \text{EI}_i,$$

where N denote the number of identified eddies in the domain shown in Fig. 1, and $\overline{\text{EI}}$ corresponds to the mean intensity of these eddies. In other words, the EAI is defined as the count of eddies multiplied by their mean intensity, or equivalently, the sum of the eddy intensities in a particular time (one week in our case).

Both these properties and the different eddy kinematics described in Section 2.1 (e.g. swirl velocity, EKE, divergence, vorticity, straining and shearing deformation rates) are computed for each detected vortex. In addition to these various properties, we also analyzed the eddy occurrence frequency and its distribution as the eddy life span and eddy characteristics along their tracks.

2.3. Eddy-tracking algorithm

Note that an "eddy" refers to a single minimum or maximum SLA center identified at a specific location and time, while an eddy track consists of the trajectory of an eddy during its lifetime. An eddy track usually lasts more than one observation interval (one week in this study) and therefore, the number of eddy tracks is usually smaller than counts of eddies. The eddy tracking algorithm used in this study is adapted from Penven et al. (2005) and minimizes a distance D between the detected eddies of two consecutive maps. For each eddy (e_1) identified on a given map at time t_1 and for each eddy (e_2) identified on the next map at time t_2 and rotating in the same sense than e_1, the nondimensional distance D_{e_1,e_2} is defined as

$$D_{e_1,e_2} = \sqrt{\left(\frac{\Delta D}{D_0}\right)^2 + \left(\frac{\Delta R}{R_0}\right)^2 + \left(\frac{\Delta \xi}{\xi_0}\right)^2 + \left(\frac{\Delta \text{EKE}}{\text{EKE}_0}\right)^2},$$

where ΔD is the spatial distance between e_1 and e_2, and ΔR, $\Delta\xi$ and ΔEKE are, respectively, the radius, the vorticity and the EKE variations between e_1 and e_2. D_0, R_0, ξ_0 and EKE_0 are, respectively, the characteristic length scale (D_0 = 100 km), characteristic radius (R_0 = 50 km), characteristic vorticity ($\xi_0 = 10^{-6}\ \text{s}^{-1}$) and characteristic EKE ($\text{EKE}_0 = 100\ \text{cm}^2\ \text{s}^{-2}$). D_{e_1,e_2} represents the degree of similarity between two eddies (smaller values indicate higher similitude between e_1 and e_2). Thus, the algorithm selects the eddy pair (e_1,e_2) that minimize D_{e_1,e_2} and considers this pair to be the same eddy that is tracked from t_1 to t_2. Since the propagation speed of the mesoscale eddies is expected to be a few tens of kilometers per week (Chaigneau and Pizarro, 2005c) and to avoid jumping from one track to another, the searched distance ΔD was restricted to 150 km. Vortices may also disappear between consecutive maps, in particular if they pass into the gaps between satellite groundtracks. To minimize this problem, we search for the same eddy for two weeks after its disappearance.

3. Comparison between the winding-angle and the Okubo–Weiss eddy identification methods

3.1. Validation protocol of the eddy identification methods

Since our goal is to automatically identify mesoscale eddies in a large volume of data, it is imperative that we validate both identification methods. The validation protocol, adapted from Segond (2006), verifies presence of the identified vortices using the following objective methodology:

(1) On the 723 available SLA maps, 10 are randomly chosen and sent to five oceanographic experts. These maps contain both the SLA field and the derived geostrophic currents.
(2) For each map, all experts draw by hand the eddy contours they identified.
(3) Their maps are then digitized and compared with the eddy contours determined by both the automated algorithms. For each map and for each vortex, rates of covering (Ae ∩ Am and Am ∩ Ae) are computed between the eddy area identified by the expert (Ae) and the corresponding area of the identification methods (Am). If one of these rates of covering are higher than a given threshold (50% in our case), the vortex is considered as correctly detected since the expert cannot determine the eddy envelop with high accuracy.
(4) Two different quantities are then estimated to validate and quantify the efficiency of both the OW and the WA eddy identification methods: the success of detection rate (SDR) and the excess of detection rate (EDR). These rates are defined as

$$\text{SDR} = \frac{N_c}{N_e},$$
$$\text{EDR} = \frac{N_{om}}{N_e},$$

where Nc corresponds to the common eddies identified by both the expert and the automated method, Ne corresponds to the total number of eddies identified by the expert and Nom (or Noe) corresponds to the number of eddies identified only by the method (or only by the expert). Note that the method can sometimes merge two close eddies identified as splitted by the expert. In this case it accounts for 1 in Nc and 1 in Noe. In contrast, if the method splits two close eddies identified as only one by the expert, both Nc and Nom are increased by 1.

3.2. Efficiency of the WA and OW methods for the detection of mesoscale vortices

Fig. 1 shows the SLA map and associated geostrophic currents for the 8th August of 2004 in the study region which extends from Northern Chile to Ecuador and from the coast to 90°W, covering a maritime area of ~2.8×10^6 km^2. Eddy contours identified by one of the experts (Fig. 1b) and by both the WA (Fig. 1c) and the OW methods (Fig. 1d) are shaded gray. This expert detected 29 eddies (N_e = 29) on this particular map (16 cyclonic and 13 anticyclonic), one more than the WA method. All the 28 structures identified by this algorithm are considered as common with the expert, but a small cyclonic vortex centered at ~14°S–78°W (Fig. 1b) is not identified by the WA method (Fig. 1c). Consequently in this example, N_c = 28, N_{oe} = 1 and N_{om} = 0, leading to an important SDR of 96.6%, and a null EDR. The WA method missed a small cyclonic eddy identified by the expert at 13.5°S and 78°W.

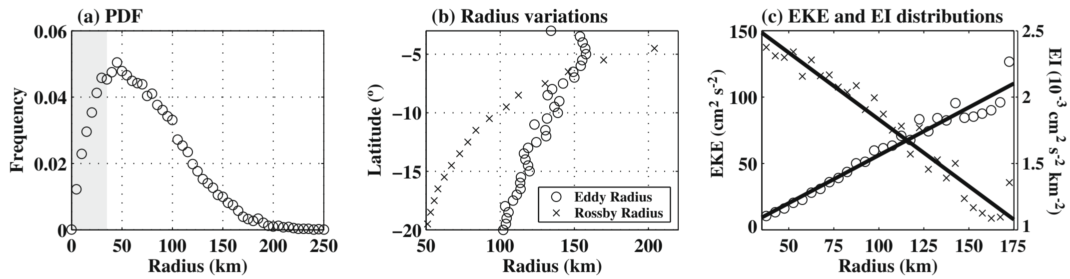

Fig. 3. Radius distributions. (a) Probability density function (PDF) of the radius sizes; The shaded region corresponds to eddy radii smaller than 35 km. (b) Meridional variation of eddy radii, for eddies with amplitude higher than 2 cm (circles); averaged Rossby radii from Chelton et al. (1998) are indicated by crosses. (c) Mean distributions of EKE (circles and left axis) and EI (crosses and right axis) as functions of eddy radii; solid lines are linear fits (for EKE, r^2 = 97.8% and an rms difference of 29.7 $cm^2\ s^{-2}\ km^{-2}$; for EI, r^2 = 97.2% and an rms difference of $0.4 \times 10^{-3}\ cm^2\ s^{-2}\ km^{-2}$).

In contrast, the OW method identified more structures than the expert. Among the 51 vortices identified by the OW algorithm, 28 structures are common with the expert ($N_c = 28$) leading to the same SDR of 96.6% obtained with the WA algorithm. However, 22 vortices are added by the OW method ($N_{om} = 22$) which leads to a strong EDR of 75.9%. The well-developed anticyclonic eddy located at the northeastern edge of the study region (Fig. 1b) is missed by the OW method ($N_{oe} = 1$). Even though we observed the same success of detection rate in both methods, the strong excess of detection of the OW algorithm in this particular example suggests a lack of efficiency of this method. But are these preliminary conclusions valid only for this particular example, or is the WA method constantly more efficient to detect vortices?

To answer, the mean detection rates (SDR and EDR) were estimated from the expert maps (50 maps in total) and the results are presented in Fig. 2a. The SDR is equivalent for both methods with mean values of 92.7% for the WA method and 86.8% for the OW algorithm. On average, only 0.8% (or 0%) of the experts' eddies are merged by the WA (or the OW) algorithm and 2% (or $\sim$ 6%) are erroneously split into two eddies. The EDR which is less than 20% for the WA method reaches 63% for the identification algorithm based on the OW parameter. With OW's EDR value of 63% and a tendency to erroneously split eddies, it is evident that the OW method over-detects. This problem was also noted by Isern-Fontanet et al. (2006) who applied the OW algorithm to vortices of the Mediterranean Sea. The SDR to EDR ratio, equivalent to a signal to noise ratio, is of 5 for the WA method and 1.4 for the OW method. These values also confirm that the automated method based on the OW parameter is not adequate to detect "true" mesoscale eddies while the WA technique is both more efficient and more conservative. Finally, although the OW algorithm identifies too many vortices, this method also fails to identify some eddies with a default of detection rate (DDR = 1 − SDR) of 13.2%. Note that the above results do not strongly depend on the choice of the selected threshold W_0 for the OW method, since the signal to noise ratio varies from 1 to 3 for W_0 varying from of $-0.05\sigma_w$ to $-\sigma_w$ (not shown). However the best compromise is effectively a W_0 value in the range $-0.3\sigma_w \leqslant -W_0 \leqslant 0.2\sigma_w$ since the success of detection rate decreases drastically outside these limits. It is also important to keep in mind that experts may, for example, miss some eddies or merge or split close eddies. As the experts do not have the possibility to correct themselves after inspection of the automatically identified eddy contours, the obtained signal to noise ratio of 5 with the WA method can be considered as a minimum value.

Finally, as the expert maps are the basis for estimating the efficiency of the automated algorithms, it is important to estimate the reliability of the expert eddy-identifications. In order to intercompare the tracking results from the different experts, Table 1 shows for each evaluated map the percentages of eddies detected by only one expert or commonly by between 2 and 5 experts. On average (last column of Table 1), 33–34 distinct eddies are identified by the experts on each given map. Around 11% of these 33 eddies are identified by only one expert whereas nearly 85% are detected by at least three of the five experts, and about 70% by all the five experts. Despite the rather good agreement between the experts, we note that 10–20% of the eddies are only identified by 1–2 experts. This suggests that 10–20% of the vortices may have a weak SLA signature and could be then considered as spurious or at least suspicious. Thus, the value of 20% can be considered as an upper limit for an acceptable error of the automated algorithms. As shown in Fig. 2, the 10–20% range is of the same order of magnitude than the DDR of both the automated methods; furthermore, the EDR of 18.7% of the WA algorithm is also in the acceptable error range set by the experts, which again confirm the good efficiency of this method compared to the OW algorithm. Thus, based on the results of this objective comparison, the WA algorithm is retained for this study and is applied to the 723 SLA maps in order to provide a reliable description and confident statistics of the mesoscale activity off Peru.

4. Mean eddy properties

4.1. Eddy radius

The probability density function of eddy radii shows a non-Gaussian distribution with a strong asymmetry (Fig. 3a). The majority of the detected eddies have a radius of $\sim$50 km and vortices with a radius higher than 175 km are very infrequent. Even if the WA algorithm can detect small-scale vortices of few km (Fig. 3a), the combination of the Lanczos filter with the truncation step size used for subsampling the alongtrack altimetric data (see Section 2.1) suggests that the SLA maps cannot correctly resolve mesoscale structures having a diameter smaller than 70 km. Hence, all the results discussed hereafter are based on vortices with radii ranging from 35 to 250 km. This restriction removes around 20% of the $\sim$25,000 vortices originally identified, but does not alter our main conclusions. The remaining cyclones and anticyclones have an average radius of 80–85 km. This mean size is relatively homogeneous over the whole spatial domain. However, considering the 35% of eddies having an SLA amplitude higher than 2 cm, Fig. 3b shows that radii increase by a factor of 1.6 from $\sim$100 km at 20°S to $\sim$160 km at 3°S. This increase is small compared to the factor of 4.5 increase in the Rossby radius of deformation (Fig. 3, 20°S vs. 3°S) that is often associated with eddy size. However, the regional study of Penven et al. (2005), performed with a high-resolution model, noted a similar equatorward increase of both the eddy radii and the characteristic eddy length-scales computed from the autocorrelation functions of surface current anomalies (Stammer, 1997). The modeled eddies exhibit typical radii of 70–80 km at 20°S and of 100–120 km at 3°S leading to a factor increase of ~1.5, similar to our observations. Other studies, based on altimetry alongtrack measurements (Stammer, 1997, 1998) or on a merged-satellite product (Chelton et al., 2007), have also identified similarly weak equatorward increases in eddy lengthscales.

The mean EKE and EI distributions as function of eddy radius are shown in Fig. 3c. The mean EKE (or EI) increases (or decreases) quasi-linearly from ~10 $cm^2\,s^{-2}$ (or from $2.5 \times 10^{-3}\,cm^2\,s^{-2}\,km^{-2}$) for eddy radii of 35 km to ~110 $cm^2\,s^{-2}$ (or to $10^{-3}\,cm^2\,s^{-2}\,km^{-2}$) for radii of 175 km. Higher discrepancies between the linear fit and the data are observed for eddy radii higher than 150 km due to a reduced number of eddies detected in this range of size (Fig. 3a). The intensity distribution is mainly explained by the relatively weak EKE range observed in the study region and the relatively large range of eddy radius. For example, eddies have a mean EKE varying of a factor 10 (from ~10 to ~100 $cm^2\,s^{-2}$) while their area vary by a factor of ~25. It is then obvious that for a same EKE range, the most energetic or most intense eddies correspond to smaller structures.

4.2. Eddy frequency

A total of 10,113 cyclones and 9842 anticyclones were identified, which corresponds to 2129 cyclone tracks and 2112 anticyclone tracks, or about 14 cyclones and anticyclones per week. These numbers indicate that there is no preference for the eddy polarity. The mesoscale structures cover an average total area of around $6.5 \times 10^5\,km^2$, representing ~25% of the study region. Fig. 4a shows the geographical distribution of the frequency of these ~20,000 identified eddies. Its interpretation is straightforward since it corresponds at every location to the percentage of time instants that the point is located within a vortex. The mean eddy frequency over the domain is of 25.7%, in agreement with the rough estimate of the mean area they cover. Mesoscale structures are commonly observed south of 15°S where eddy frequency is of order of 30–50% but also offshore of Chimbote at around 9°S–82°W (Fig. 4a). These regions also correspond to local maxima in EKE of order of 100–150 $cm^2\,s^{-2}$ (Fig. 4c). The mean spatial correlation between the eddy frequency and EKE distributions decreases from 40% south of 12°S to less than 20% in the 8°S–12°S latitude band (not shown). North of 8°S, the eddy frequency decreases to 20–25% (Fig. 4a and b) whereas EKE values are higher than 200 $cm^2\,s^{-2}$ (Fig. 4c). In this northern region, the two fields are anticorrelated at −20% which suggests than the high SLA variance observed north of 8°S is rather associated with equatorial long-wave dynamics than energetic mesoscale eddies. Strong minima of eddy occurrence, with values weaker than 5–10%, take place all along the coast. The reason is that eddies are not fully developed in these coastal regions so that the WA algorithm cannot find closed streamlines. Finally, no significant difference was observed between the distribution of cyclonic and anticyclonic eddy frequencies nor in terms of seasonal variability.

4.3. Eddy lifespan

The lifespan distribution of the 4241 eddy trajectories is shown in Fig. 5a. The average lifetime of an eddy is 33 days and the median lifetime is of 14 days, without important difference between the two types of eddies. The seasonal variation of mean eddy lifespan was also insignificant with values of 33–35 days all year. For lifetimes shorter than 2 months, eddy numbers exhibit steep declines (Fig. 5a). Longer lifetimes are well approximated by expo-

Table 1
Percentage of eddies identified by only one expert and commonly by between 2 and 5 experts for each evaluated map. Numbers into brackets denote the number of distinct identified eddies.

	Map #1 (32)	Map #2 (37)	Map #3 (31)	Map #4 (31)	Map #5 (28)	Map #6 (38)	Map #7 (35)	Map #8 (36)	Map #9 (32)	Map #10 (33)	Average (33.3 ± 3.1)
1 expert	9.4	21.6	16.1	16.1	0	2.6	11.4	11.1	9.4	12.1	10.9 ± 6.3
2 experts	6.2	2.7	6.5	12.9	7.1	5.3	2.9	8.3	3.1	6.1	6.1 ± 3.1
3 experts	3.1	5.4	6.5	3.2	0	5.3	11.4	5.6	0	6.1	4.7 ± 3.3
4 experts	6.2	13.5	3.2	3.2	7.1	13.2	14.3	5.6	6.2	21.2	9.4 ± 5.9
5 experts	75.1	56.8	67.7	64.6	85.8	73.6	60.0	69.4	81.3	54.5	68.9 ± 10.3

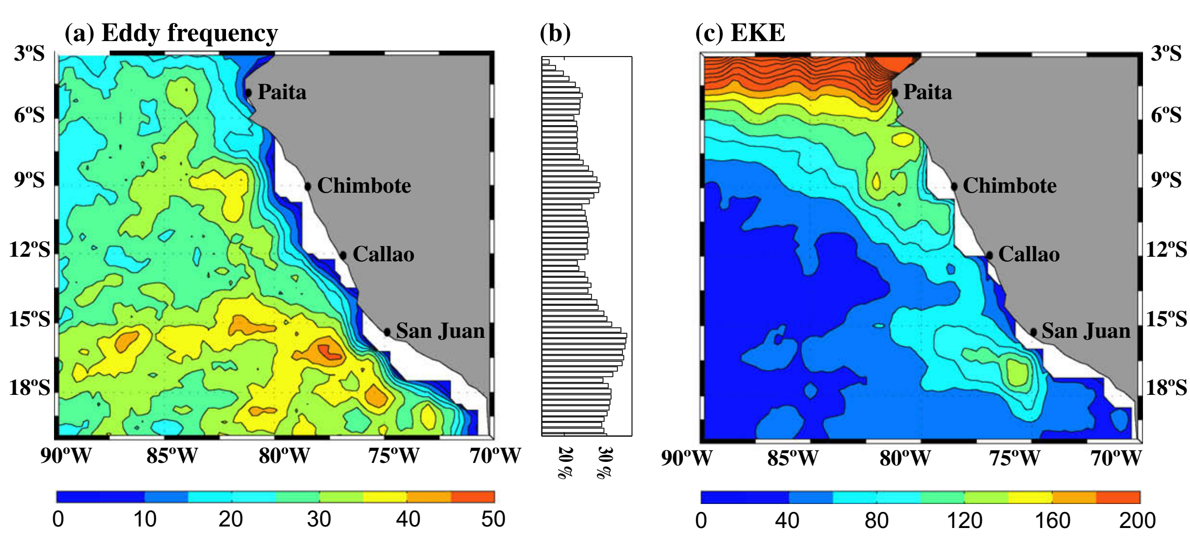

Fig. 4. (a) Mean regional climatology of eddy frequency (in %) for October 1992–August 2006. (b) Meridional variations of mean eddy frequencies (in %). (c) Spatial distribution of mean EKE (in $cm^2\,s^{-2}$) from satellite altimeter measurements.

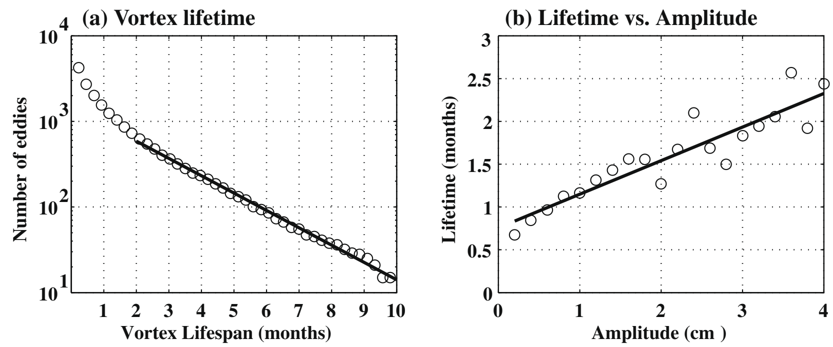

Fig. 5. (a) Vortex lifespan distribution (black circles, logarithmic scale); heavy line is a linear fit (r^2 = 99.6% and an rms difference of 12 days). (b) Variation of vortex lifespan as function of eddy amplitude; heavy line is a linear fit (r^2 = 91.8% and an rms difference of 6 days).

nentially decaying distributions (black solid line in Fig. 5a) with a correlation coefficient of 99.7% and a root mean square (rms) difference of 12 days. This distribution implies constant probability for surviving an additional week (month) of 90% (67%). In order to assess the dependence of survivability on eddy strength, we calculate 7-day survival probabilities for tracks lasting at least 2 months as function of EI (not shown). Survival probabilities increase from 85% for eddy intensities weaker than $10^{-3}\,cm^2\,s^{-2}\,km^{-2}$ to 92% for intensities higher 3×10^{-3} $cm^2\,s^{-2}\,km^{-2}$. Another monotonic relationship is observed between eddy lifetimes and eddy amplitudes at the time they are formed (Fig. 5b). Eddy lifespan increases on average from less than 1 month for a very weak eddy having "birth amplitude" of 0.5 cm to 2–3 months for a more developed eddy having initial amplitude higher than 3 cm. However, no interesting relationship was found between "birth intensity" and eddy lifespan. Finally, eddy lifetimes not only depend on their amplitude but also on their place of birth, showing a clear dependence with the latitude: eddies generated south of 15°S have a mean lifetime of 50–60 days, whereas eddies formed north of 5°S exist for an average of 10–15 days. This short near-equator lifespan also confirms that the high EKE values observed in the northern part of the study region (Fig. 4c) are not associated with eddies but rather with other processes such as equatorial long-waves or tropical instability waves.

4.4. Eddy kinematics

Table 2 shows the statistics of eddy kinematic parameters over the study region. Cyclonic and anticyclonic eddies have similar average vorticities of order of $2.5 \times 10^{-6}\,s^{-1}$ in absolute value. On average, the shearing and stretching deformations rates and the divergences of both types of eddies are several order of magnitude smaller than the vorticities. However, a total deformation rate of $\sim 10^{-6}\,s^{-1}$ suggests than eddies tend to be deformed and are not perfectly circular. Fig. 6a shows the distribution of both the vorticity and the total deformation rate as function of EI. The total deformation increases by a factor 4 from around 0.6×10^{-6} to $2.4 \times 10^{-6}\,s^{-1}$ whereas the vorticity increases by a factor 6 from 1×10^{-6} to $6 \times 10^{-6}\,s^{-1}$. As the ratio between the deformation rate and the vorticity decreases from 0.6 to 0.4, the most intense eddies should be less deformed and more circular. To verify this hypothesis and better investigate the eddy shape, we use the least squares method to fit ellipses to the ~20,000 eddy edges. The non-circular shape of these vortices is confirmed by a mean ellipse eccentricity of 1.65 for both types of eddies. As expected, the mean ellipse eccentricity slightly decreases with the EI (Fig. 6b): weakly intense eddies (EI < $0.8 \times 10^{-3}\,cm^2\,s^{-2}\,km^{-2}$) have an eccentricity of more than 1.7 whereas strong energetic eddies (EI > $4 \times 10^{-3}\,cm^2\,km^{-2}$) are more circular with a mean eccentricity of ~1.55.

Finally, other kinematics properties have been studied such as the mean distribution of the rotation velocity or of the EKE across eddies. Average swirling velocities V_θ increase outward to a maximum of around 10 cm s^{-1} at the eddy edges (not shown), in agreement with the results of Chaigneau and Pizarro (2005c) obtained from surface drifters and altimetry measurements. EKE which is negligible at the eddy center also increases outward to a mean value of ~70 $cm^2\,s^{-2}$ at the eddy edges. However, averaged values of EKE inside the detected eddies are relatively small with values of $37 \pm 69\,cm^3\,s^{-2}$ for cyclonic eddies and $42 \pm 59\,cm^2\,s^{-2}$ for anticyclones.

Section 4 has been devoted to a detailed investigation of mean eddy properties (radius, frequency, lifetime and kinematics) in the study region. We will now focus in Section 5 on the genesis and on the propagation mode of "non-stationary" eddies. Section 5 also deals with the evolution of the characteristics of long-lived eddies (radius, amplitude, intensity and vorticity).

Table 2
Mean statistics of the eddy kinematics for the time period October 1992–August 2006.

	Mean	Standard deviation	Minimum	Maximum
10,113 Cold-Core Cyclonic eddies (Unit: $10^{-6}\,s^{-1}$)				
Vorticity	−2.523	1.165	−17.392	−0.525
Shearing deformation	0.047	0.846	−6.330	6.840
Stretching deformation	0.115	0.872	−5.424	6.377
Total deformation	1.001	0.700	0.010	6.875
Divergence	5×10^{-5}	0.006	−0.235	0.079
9842 Warm-Core Anticyclonic eddies (Unit: $10^{-6}\,s^{-1}$)				
Vorticity	2.449	1.272	0.528	21.724
Shearing deformation	−0.044	0.836	−7.570	4.588
Stretching deformation	−0.009	0.847	−5.190	4.625
Total deformation	0.968	0.693	0.006	7.571
Divergence	-1×10^{-5}	0.006	−0.137	0.076

5. Eddy life cycles

5.1. Genesis and propagation

The geographical distribution of the points of eddy genesis is presented in Fig. 7 in color shading. The location of genesis corresponds to the initial point of an eddy track having a minimum lifetime of 1 month. This threshold on the lifespan is imposed to select only the "non-stationary" or propagating eddies. Eddy genesis is more frequent near the coast than in the interior ocean, with five

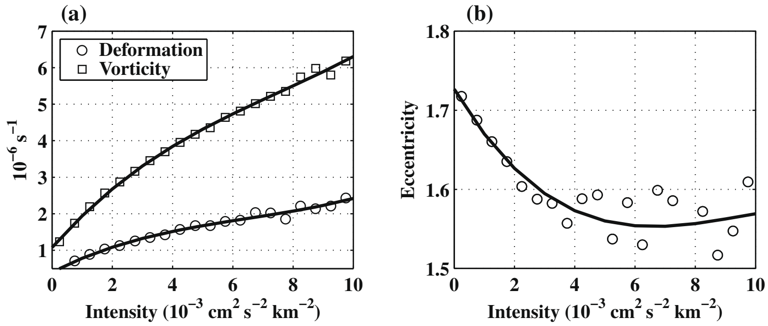

Fig. 6. (a) Eddy vorticity (black squares) and total deformation rate (black circles) as functions of EI; Solid lines shows third-order polynomial fits (for vorticity, r^2 = 99.9% and an rms difference of 7.9×10^{-8} s^{-1}; for deformation rate r^2 = 99.3% and an rms difference of 6.6×10^{-8} s^{-1}). (b) Variation of fitted ellipse eccentricity (no unit) as function of EI; Solid line shows third-order polynomial fit (r^2 = 85.8% and an rms difference of 0.03).

pronounced maxima nearshore between 6°S and 20°S. The temporal variations of eddy genesis are examined in further detail in Section 6. The coastal formation of eddies may be due to interactions of the Peru–Chile Current system with the coastline, presence of the strong upwelling front, or the high-temporal variability of the coastal flow (Pizarro et al., 2002). The intensification of the poleward subsurface Peru–Chile Undercurrent by the downwelling Kelvin waves of equatorial origin can also destabilize the near-surface coastal circulation (Shaffer et al., 1997; Zamudio et al., 2001) and generate eddies. Despite these pronounced maxima along the coast, eddy genesis also occurs offshore (Fig. 7). Additional localized maxima of eddy genesis with weaker amplitudes appear for instance in the entire region between 9°S and 14°S.

Fig. 7 also displays the mean eddy velocity propagation field (black arrows) computed by a centered difference scheme at each 7-day eddy displacement. Eddies propagate offshore quasi zonally over the entire study region, except north of 9°S where a southwestward component is observed. On average, eddy propagation velocities increase equatorward from a mean value of around 3 cm s^{-1} at 20°S to 5–6 cm s^{-1} north of 9°S, substantially weaker than the eddy-edge swirl velocities of ~10 cm s^{-1} (see Section 4.4). This velocity difference confirms eddy coherence with a clear separation between the rotating core and the surrounding advective flow. These eddy propagation velocities of 3–6 cm s^{-1} are of the same order of the estimates of Chaigneau and Pizarro (2005c); the northward increase in velocity is consistent with the meridional changes of eddy motions on a β-plane (Cushman-Roisin, 1994). However, the observed eddy propagation speeds are systematically lower than both the energetic large-scale Rossby wave zonal wave speeds of 10–30 cm s^{-1} (Maharaj et al., 2005; Chelton et al., 2007) and the westward South-Equatorial Current of ~8 cm s^{-1} observed in the region from near-surface drifter measurements (Chaigneau and Pizarro; 2005b). Thus, as also mentioned by Chelton et al. (2007), the observed SLA variability at these low latitudes consists of a superposition of fast-propagating Rossby waves and slowly-propagating mesoscale eddies. Differences between cyclonic and anticyclonic eddy pathways of long-lived vortices are investigated in Section 5.2.

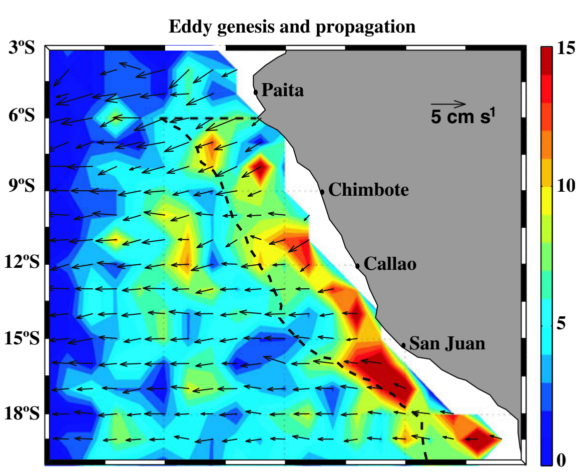

Fig. 7. Regional climatology of eddy genesis, October 1992–August 2006. Units are number of events. Only eddies having a lifetime higher than 1 month are included. Average motion vectors for eddy centers are superimposed (black quivers). Bold dashed lines delimit the "coastal region" where temporal eddy characteristics variations are investigated in Section 6 and Figs. 9 and 10.

5.2. Growth and decay of long-lived eddies

Average eddy characteristics over 6-months of life are shown in Fig. 8. This analysis is based on 32 (or 39) long-lived cyclonic (or anticyclonic) eddies. Both types exhibit similar growth rates in terms of radius and SLA amplitude (Fig. 8a and b). Long-lived eddy radii increase at a rate of ~12–15 km per month whereas the amplitudes grow by ~1 cm per month. The growth phase of 3 months is however shorter for anticyclonic eddies, with a maximum mean radius of 100 km and amplitude of ~4 cm. In contrast, cyclonic eddies are fully developed after a growing phase of 4 months, with typical radii of 120 km and SLA amplitudes of 4.5 cm. The decay phases of the two eddy types are also distinct. After 3–4 months of propagation, anticyclonic eddies tend to maintain their size whereas their amplitudes decay (~2 cm). In contrast, cyclonic eddies decay slowly in terms of SLA amplitude (Fig. 8b) but rapidly decrease in size (Fig. 8a). After 6 months of propagation the SLA amplitudes of cyclones are still two times higher (~4 cm) than at the time of their genesis (~2 cm). Finally, the temporal evolution of the mean energy density also depends on direction of rotation (Fig. 8c). While the intensity of anticyclonic vortices decays quasi-linearly by about 70% in 180 days, the cyclones intensity decays by 50% during the first 80 days before reaching a near-constant value of 1.8×10^{-3} cm^2 s^{-2} km^{-2}. Further investigation is needed to determine the physical processes involved in these differing evolutions, but similar differences in eddy characteristics have been observed for atmospheric vortices (Hakim and Canavan, 2005).

Fig. 8d shows the average meridional propagation of long-lived eddies. During the first 50 days, eddies formed near the coast propagate offshore remaining close to their latitude of birth. After this period however, a clear separation is observed: cyclonic eddies continue westward during four more months before turning slightly southward, whereas anticyclonic eddies move preferentially northwestward with a meridional displace-

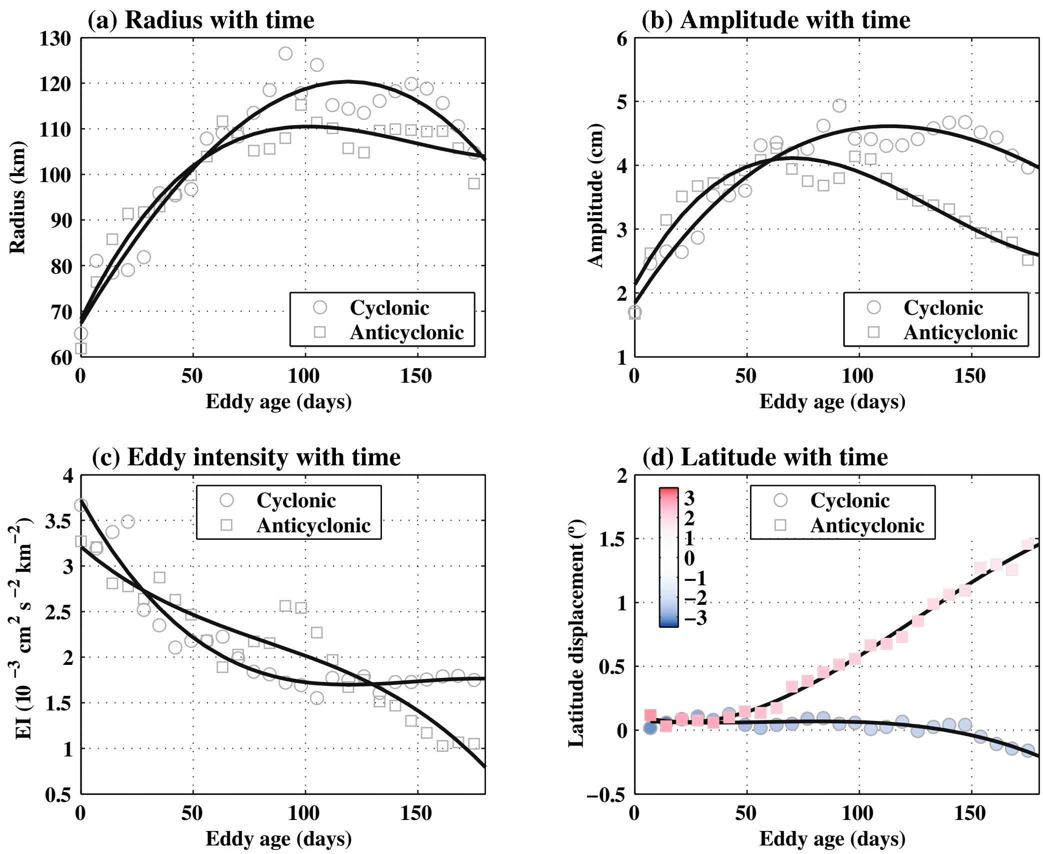

Fig. 8. Ensemble-mean properties of long-lived eddies over 180 days: (a) radius, (b) amplitude, (c) intensity, and (d) latitude. Cyclonic eddies are depicted by circles and anticyclonic eddies by squares. Solid lines are third-order polynomial fits. Colours in (d) show the evolution of vorticity (in $10^{-6}\ s^{-1}$). All included vortices survived a minimum of 180 days so that the population is constant for all times displayed.

ment rate of 1.5° in 4 months corresponding to a northward velocity component of ~10 km per week. After 6 months, both types of eddies have traveled 750 km offshore (not shown) but anticyclonic vortices are found on average 1.7° further north than the cyclones. This divergence in eddy pathways, related to the β effect (Cushman-Roisin, 1994), has been previously observed in the ESP (Chaigneau and Pizarro, 2005c), in other eastern boundary current systems (Morrow et al., 2004b) and in the global ocean (Chelton et al., 2007). Pathway divergence may have important repercussions in tracer budgets, leading for example to a net equatorward heat transport. Finally, as the warm anticyclonic (or cold cyclonic) eddies move equatorward (or poleward) they are subject in the southern hemisphere to a higher (or lower) planetary vorticity *f*. In order to maintain their absolute vorticity, their relative vorticity ξ may decrease (or increase). As shown in Fig. 8d, the relative vorticity of long-lived anticyclones, averaged over the eddy area, decreased in average from 3.3×10^{-6} to $1.7 \times 10^{-6}\ s^{-1}$ after 6 months. In contrast, the relative vorticity of long-lived cyclones increased from an averaged value of -3.5×10^{-6} to $-2.2 \times 10^{-6}\ s^{-1}$. However, even considering the vorticity of the mean large-scale circulation, the temporal evolution of the absolute vorticity ($\xi + f$) does not remain constant, which suggests that the vertical eddy extent may also change during the vortex propagation, in order to conserve the potential vorticity.

Section 5 has given results on the locations of eddy genesis, on the propagation modes and on the life-cycle of long-lived eddies. However, the relatively high-temporal resolution of the altimetry dataset also allows temporal variability of eddies to be examined, since 1992. The next section examines temporal variations at seasonal and interannual scales.

6. Temporal evolution of the mesoscale eddy characteristics

In this section, we consider the ~4500 eddies located south of 6°S and less than 4° offshore the South-American coast. This sub-domain corresponds to the main region of eddy genesis (see black dashed line in Fig. 7); the temporal variations discussed below concern the newly-formed or "young" eddies of this region.

6.1. Seasonal cycle

Fig. 9 shows the mean seasonal cycle of coastal eddy properties. The number of coastal eddy and their size do not significantly vary seasonally, with values of 5.7–6.1 generated eddies per week having mean radii of 77–81 km year around (Fig. 9a and b). In contrast, SLA amplitudes (Fig. 9c) between eddy centers and eddy edges are 25% higher during fall (~2.1 cm) than during spring (~1.7 cm). The combination of increase SLA gradients and unchanged radii results in higher levels of EKE and EI during fall (Fig. 9d and e). The EKE and EI are, respectively, 45% and 50% stronger during this season than spring. Finally, as eddies are slightly more numerous and more intense during fall, the EAI is also maximal during this season (Fig. 9f). During fall, mesoscale vortices are ~35% more active than in summer and winter and 65% more active than in spring.

The enhanced EI and eddy activity during fall may be related to the strength of the thermal front separating the cold upwelled coastal water from warmer offshore water. Firstly, the annual amplitudes of both the sea-surface temperature (SST) and the upper layer heat content are maximal around 300–500 km offshore and minimal along the coast (Takahashi, 2005). Due to the ocean's

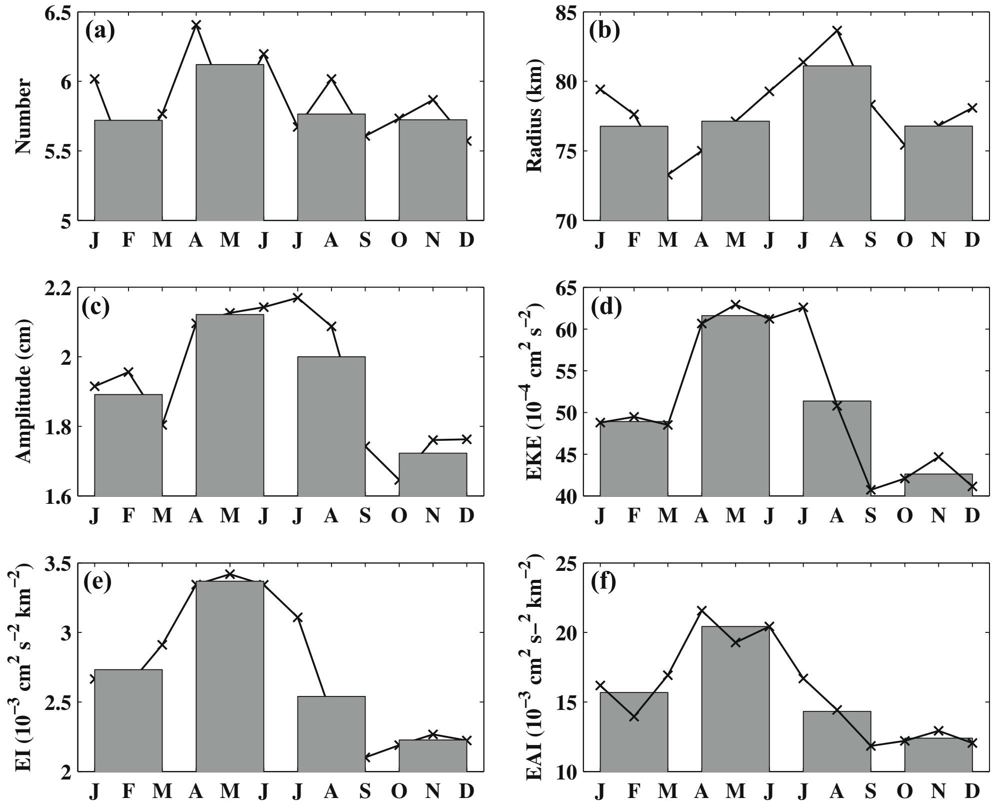

Fig. 9. Seasonal cycles of newly-formed coastal eddies: (a) number of eddies, (b) radius (km), (c) amplitude (cm), (d) EKE (cm^2 s^{-2}), (e) EI (10^{-3} cm^2 s^{-2} km^{-2}), and (f) EAI (10^{-3} cm^2 s^{-2} km^{-2}). Vertical bars indicate seasonal (3-month) averages whereas black lines show the monthly variations.

thermal inertia, the mean SST reaches its maximum value between March and May (Mitchell and Wallace, 1992) producing strong zonal SST gradients with an associated strong thermal front during this period. Based on 3 years of remote sensing data, Carr et al. (2002) observed that the maximal frontal gradients along the Peruvian coast take place in later summer and fall. Secondly, frontal intensity is also reinforced at the end of summer by a stronger inshore advection of equatorial and subtropical waters (Grados, 1989; Vázquez and García, 2001), principally observed near Chimbote (9°S) and between 15°S and 20°S (Grados, 1989; Takahashi, 2005). This latter region also corresponds to the northern limit of the cold Chile–Peru Current which turns westward at about 9°S to feed the South-Equatorial Current (Strub et al., 1998; Chaigneau and Pizarro, 2005b). The seasonal variations of frontal intensity driven by atmospheric fluxes and advective processes could thus enhance generation of baroclinic instabilities during fall and could explain the seasonal variations observed in Fig. 9. However, this interpretation requires further investigation, probably with satellite SST data, historical in-situ hydrographic data and a high-resolution regional model.

6.2. Interannual variations

To remove the intraseasonal and seasonal fluctuations of eddy properties and investigate only interannual variations, we applied a one-year running-mean to the original time-series (Fig. 10). The study time period (1992–2006) includes the years when only T/P data alone were available (December 1993–March 1995; see Section 2.1) and distinct phases of warm (or cold) El Niño Southern Oscillation associated with El Niño (or La Niña). Within the period of altimetry measurements, a very strong El Niño occurred in 1997–1998 followed by a weak event in 2002–2003 (ENFEN, 2003). In contrast, relatively cold La Niña events took place in 1995–1996 and 1998–2000 (McPhaden, 2006).

During the T/P alone period, eddies appear less numerous (Fig. 10a) with weakened SLA amplitude (Fig. 10c), leading to slightly less energetic and intense eddies (Fig. 10d and e). The EAI was consequently reduced by 35% during this period (Fig. 10f). As mentioned in Section 2.1, the coarse resolution of T/P groundtracks (typically 200–300 km in the study region) leads, on average over the World Ocean, to a reduction in EKE of 30%. In the study area, the EKE decreases by 20% from a local maximum of $\sim$ 45 cm^2 s^{-2} in summer of 1994 to a minimum of $\sim$35 cm^2 s^{-2} in summer of 1995. In contrast, during the strong El Niño period both the eddy amplitude, the EKE and the EI are strongly increased. However the combination with a relatively weak number of eddies (Fig. 10a) does not lead to an exceptional peak in the EAI in 1997–1998. During the strong El Niño period, the EAI is of $\sim 22 \times 10^{-3}$ cm^2 s^{-2} km^{-2}, 40% higher than the mean value observed between 1992 and 2006. These observed variations were not reproduced during the weak El Niño event of 2002–2003 which was associated with rather weak EAI values of $\sim 15 \times 10^{-3}$ cm^2 s^{-2} km^{-2}. This may indicate that the 2002–2003 event did not significantly impact on the oceanographic conditions along the Peruvian coast. During the relatively cold La Niña period of 1995–1996, eddy SLA amplitudes and the EAI also exhibit weak values, but we cannot provide any strong conclusion since this period includes the summer of 1995 where ERS-1 data is not available. Furthermore this relatively weak eddy activity period was not reproduced during La Niña event of 1998–2000. Finally, an increase of the EAI was observed for a one-year period starting in winter of 2004 (Fig. 10f) associated with an increase number of vortices during this period (Fig. 10a). The maximum EAI values observed in spring 2004 (October–November) coincides with reduced

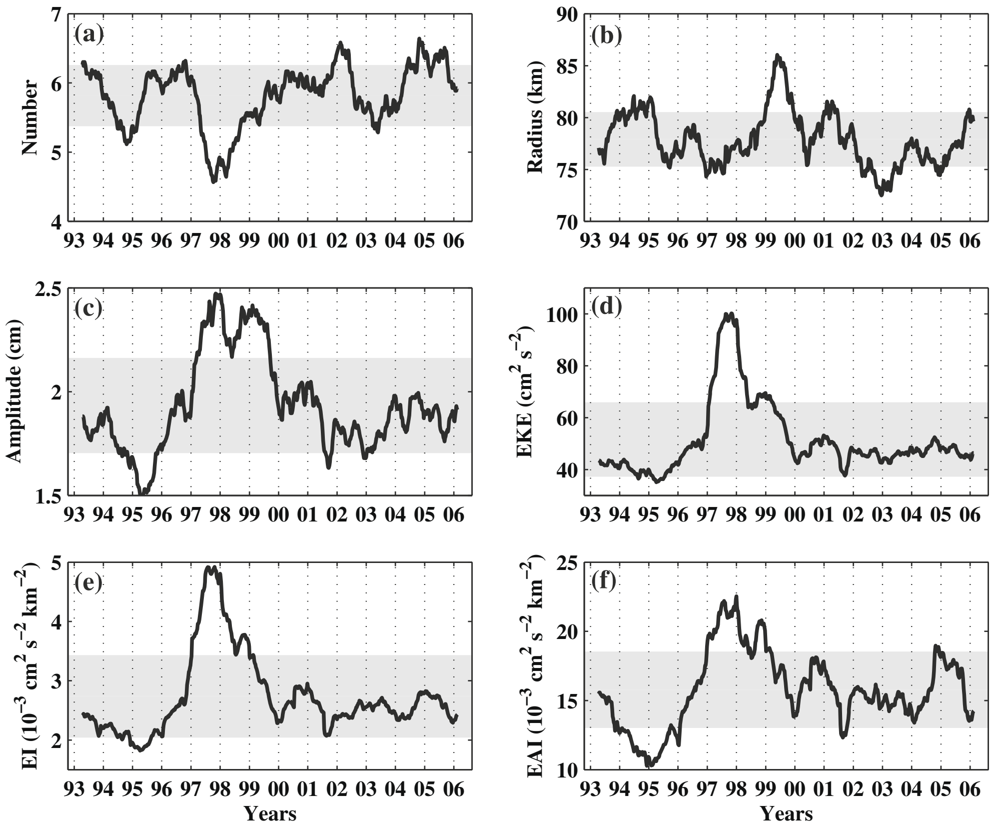

Fig. 10. Interannual variations of newly-formed coastal eddies, October 1992–August 2006: (a) number of eddies, (b) radius (km), (c) amplitude (cm), (d) EKE (cm^2 s^{-2}), (e) EI (10^{-3} cm^2 s^{-2} km^{-2}), and (f) EAI (10^{-3} cm^2 s^{-2} km^{-2}). Average values ± one standard deviation shaded in gray. These interannual variations have been computed through a one-year running-mean of the original data.

upwelling areas and an important inshore advection of warmer and saltier subtropical waters from Chimbote to 16°S (IMARPE, 2005). This local scenario was the consequence of the southward propagation of a coastal-trapped wave forced at the equator by a large-scale equatorial Kelvin wave. However, the physical mechanisms responsible of the observed eddy activity variations at interannual scales are not completely understood and further investigation is needed.

7. Summary and future work

This study investigates the eddy population off Peru using nearly 15 years of satellite altimetry measurements with high spatio-temporal resolution. The first part compares two distinct automated eddy identification methods. When considering that "*a vortex exists when instantaneous streamlines mapped onto a plane normal to the vortex core exhibit a roughly circular or spiral pattern* (...)" (Robinson, 1991), the geometrical method using the streamline function curvatures to identify eddies appears much more efficient than the algorithm based on the value of the Okubo–Weiss parameter. With a success of detection/excess of detection ratio of 5, we strongly recommend the use of the "winding-angle" method for the detection of eddy edges.

A second part provides an analysis of the mean eddy properties offshore the Peruvian coast. Around 14 cyclonic and 14 anticyclonic eddies with radii higher than 35 km were identified on each weekly map, providing more than 20,000 eddies to be studied (October 1992–August 2006). In general, no significant difference is observed between cyclonic and anticyclonic eddies in terms of mean characteristics, occurrence frequency and formation region. The typical size of the well-developed eddies having amplitudes higher than 2 cm increases equatorward from a minimum value of ~100 km at 20°S to a maximum of ~160 km north of 5°S. However, considering all eddies, their mean radius is ~80 km and mean lifetime ~1 month. They also exhibit a time-independent 1-week survival probability of 90%, for lifetimes greater than around 2 months. Eddies, which are more frequently observed south of 15°S and offshore Chimbote (9°S) than in the rest of the study domain, are rather coherent since the vorticity/total deformation ratio increases from 1.5 to 2.5 with increase EI.

Long-lived eddies are principally formed near the coast and propagate offshore at mean speeds of 3–6 cm s^{-1}. During the first 3–4 months of westward propagation, cyclonic and anticyclonic long-lived eddies exhibit a growing phase where both their radii and SLA amplitudes increase by a factor ~2–3. Then, both types of eddies show a decaying phase impacting the amplitudes of anticyclonic and the sizes of the cyclonic vortices. However in terms of EI (e.g. energy density), cyclonic eddies show a rapid decay during the first 3 months before stabilizing at a quasi-constant value, whereas anticyclones exhibit a regular decline. Finally, the displacement of long-lived eddies confirm the divergence observed in previous studies (Morrow et al., 2004b; Chaigneau and Pizarro, 2005c): anticyclonic eddies propagate preferentially northwestward while cyclonic eddies migrate in the southwestward direction. During propagation their relative vorticities increase in response to latitudinal changes in planetary vorticity.

Temporal variations of the most energetic eddies show an important variability at seasonal scales. Eddies are slightly more numerous and intense in fall, leading to a strong EAI. This EAI, 65% stronger in fall than during spring, may be related to seasonal variations of the thermal front intensity. At interannual scales, eddy activity and eddy characteristics in general are strongly decreased in 1994–1995 due to inconsistency of the data set, being affected by the T/P alone measurements. In contrast, the EAI reaches its maximum value during the strong El Niño event of 1997–1998 and another clear maximum is observed at the end of 2004 possibly due to the passage of a coastal-trapped wave.

The results may be useful for the validation of high-resolution regional models and could be of interest to the biological community to investigate links between ecosystems and mesoscale activity along the highly productive Peruvian coast. However, owing to limited resolution and necessary interpolation, the altimetry mapped data impose space and timescale limitations and miss small-scale vortices. In particular, based on satellite-tracked drifter trajectories, Chaigneau and Pizarro (2005c) have shown than the typical eddy radius of the ESP is about 20 km, and that 70% of eddies have a radius smaller than 35 km. Thus once validated, regional models could help to document, for example, the impacts of smaller vortices on the offshore transport of coastal water properties, on physical budgets (heat, salt, mass, etc.), and on productivity and ecosystems.

The results also raise a number of additional questions that require future research. For example, the respective roles of local versus remote forcing of equatorial origin on eddy genesis and the effects of this forcing on both cyclonic and anticyclonic vortices. Similarly, general mechanisms contributing to the growth and decay of eddies need be examined in detail. Another unresolved problem concerns the merging of eddies which can be an important process to the vortex phenomenology. The particular case of dipolar eddies should also be investigated since convergence/divergence lines between eddies, by analogy of the Rossby wave–induced convergences, could have important repercussions on the distribution of living organisms (e.g. Dandonneau et al., 2003). Finally, the impact of large-scale warming on mesoscale activity needs be evaluated. Attempts at reliable objective classification of these processes will likely require high-resolution regional models forced by realistic atmospheric fields.

Acknowledgements

The authors would like to thank B. Dewitte, G. Eldin, M. Lengaigne, R. Morrow and O. Pizarro, whose expertise has been valuable for the validation of the automated methods. We are also grateful to the two reviewers, K. Takahashi and D. Chelton, for constructive comments. A. Gizolme was supported by the Interdepartmental Thematic Action « Humboldt Current System » from IRD and by the « Peru Chile Climate Change » project funded by the Agence Nationale de la Recherche.

Appendix A. Appendix

As explained in Section 2.2, the winding-angle eddy identification algorithm attempts to locate a vortex by selecting and clustering closed streamlines (Guo, 2004). Let us consider a 2D streamline beginning at a starting point P_1 (Fig. 11) and composed of several segments which the length corresponds to the step size (around 1.35 km in our case). The winding-angle (WA) of the streamline corresponds to the cumulated sum of the angles between all pairs of consecutive segments

$$\mathrm{WA} = \sum_{j=2}^{N-1} \langle P_{j-1}, P_j, P_{j+1} \rangle = \sum_{j=2}^{N-1} \alpha_j,$$

where $\langle P_{j-1}, P_j, P_{j+1} \rangle = \alpha_j$ denotes the signed angle between the segments $[P_{j-1}P_j]$ and $[P_jP_{j+1}]$. Positive values of α correspond to counterclockwise-rotating curves and negative values correspond to clockwise-rotating curves.

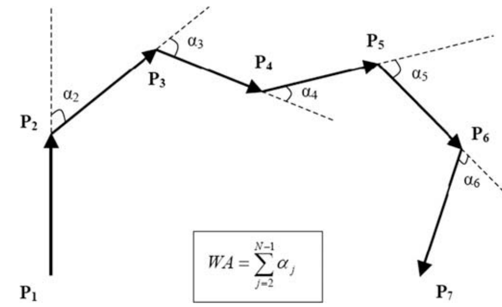

Fig. 11. Winding-angle (WA) schematic representation for a segmented streamline.

In the WA eddy identification method, a streamline is associated with an eddy if its winding-angle is higher than 2π.

References

Bakun, A., 2006. Fronts and eddies as key structures in the habitat of marine fish larvae: opportunity, adaptive response and competitive advantage. Scientia Marina 70 (2), 105–122.

Basdevant, C., Philipovitch, T., 1994. On the validity of the "Weiss criterion" in two-dimensional turbulence. Physica D 113, 17–30.

Bryan, K., 1996. The role of mesoscale eddies in the poleward transport of heat by the oceans: a review. Physica D 98, 249–257.

Buning, P., 1989. Numerical Algorithms in CFD Post-Processing. In: Computer Graphics and Flow Visualization in Computational Fluid Dynamics. Lecture Series 1989–07. Von Karman Institute for Fluid Dynamics, Brussels, Belgium.

Carr, M.-E., Strub, P.T., Thomas, A.C., Blanco, J.L., 2002. Evolution of 1996–1999 La Niña and El Niño conditions off the western coast of South America: a remote sensing perspective. Journal of Geophysical Research – Oceans 107 (12), 3236. doi:10.1029/2001JC001183.

Chaigneau, A., Pizarro, O., 2005a. Surface circulation and fronts of the South Pacific Ocean, east of 120°W. Geophysical Research Letters 32, L08605. doi:10.1029/2004GL022070.

Chaigneau, A., Pizarro, O., 2005b. Mean surface circulation and mesoscale turbulent flow characteristics in the eastern South Pacific from satellite tracked drifters. Journal of Geophysical Research – Oceans 110, C05014. doi:10.1029/2004JC002628.

Chaigneau, A., Pizarro, O., 2005c. Eddy characteristics in the eastern South Pacific. Journal of Geophysical Research – Oceans 110, C06005. doi:10.1029/2004JC002815.

Chavez, F.P., 1995. A comparison of ship and satellite chlorophyll from California and Peru. Journal of Geophysical Research – Oceans 100 (C12), 24855–24862.

Chelton, D.B., Schlax, M.G., 2003. The accuracies of smoothed sea surface height fields constructed from tandem satellite altimeter datasets. Journal of Atmospheric and Oceanic Technology 20, 1276–1302.

Chelton, D.B., de Szoeke, R.A., Schlax, M.G., El Naggar, K., Siwertz, N., 1998. Geographical variability of the first-baroclinic Rossby radius of deformation. Journal of Physical Oceanography 28, 433–460.

Chelton, D.B., Schlax, M.G., Samelson, R.M., de Szoeke, R.A., 2007. Global observations large oceanic eddies. Geophysical Research Letters 34, L15606. doi:10.1029/2007GL030812.

Cushman-Roisin, B., 1994. Introduction to Geophysical Dynamics. Prentice-Hall, Upper Saddle River, NJ. 320 pp.

Dandonneau, Y., Vega, A., Loisel, H., du Penhoat, Y., Menkes, C., 2003. Oceanic Rossby waves acting as a "hay rake" for ecosystem floating by-products. Science 302, 1548–1551.

Ducet, N., Le Traon, P.Y., Reverdin, G., 2000. Global high-resolution mapping of ocean circulation from TOPEX/Poseidon and ERS-1 and -2. Journal of Geophysical Research – Oceans 105, 19477–19498.

ENFEN, 2003. Informe Técnico ENFEN-Enero 2003, Comité Multisectorial para el Estudio Nacional del Fenómeno El Niño <http://www.imarpe.gob.pe>.

Falkowski, P.G., Zieman, D., Kolber, Z., Bienfang, P.K., 1991. Role of eddy pumping in enhancing primary production in the ocean. Nature 352, 55–58.

Fang, F., Morrow, R., 2003. Evolution, movement and decay of warm core Leeuwin Current eddies. Deep-Sea Research II 50, 2245–2261.

Grados, C., 1989. Variabilidad del regimen hidrico del codo Peruano–Chileno. Comisión Permanente del Pacifico Sur, Revista del Pacifico Sur (numero especial), 95–104.

Guo, D., 2004. Automated feature extraction in oceanographic visualization. Master Thesis, Massachusetts Institute of Technology, unpublished.

Hakim, G.J., Canavan, A.K., 2005. Observed cyclone–anticyclone tropopause vortex asymmetries. Journal of Atmospheric Sciences 62, 231–240.

Helly, J.J., Levin, L.A., 2004. Global distribution of naturally occurring marine hypoxia on continental margins. Deep-Sea Research I 51, 1159–1168.

Hormazabal, S., Shaffer, G., Leth, O., 2004. Coastal transition zone off Chile. Journal of Geophysical Research – Oceans (109), C01021. doi:10.1029/2003JC001956.

Hussain, F., Huyakawa, M., 1987. Education of large-scale organized structure in a turbulent plane wake. Journal of Fluid Mechanics 180, 193–204.
IMARPE, 2005. Informe Anual de Metas 2004 de la Unidad de Oceanografía Física. Internal report, unpublished.
Isern-Fontanet, J., García-Ladona, E., Font, J., 2003. Identification of marine eddies from altimetry. Journal of Atmospheric and Oceanic Technology 20, 772–778.
Isern-Fontanet, J.I., Font, J., Garcia-Ladona, E., Emelianov, M., Millot, C., Taupier-Letage, I., 2004. Spatial structure of anticyclonic eddies in the Algerian basin (Mediterranean Sea) analyzed using the Okubo–Weiss parameter. Deep-Sea Research I 51, 3009–3028.
Isern-Fontanet, J.I., García-Ladona, E., Font, J., 2006. Vortices of the Mediterranean Sea: an altimetric perspective. Journal of Physical Oceanography 36, 87–103.
Jayne, S.R., Marotzke, J., 2002. The oceanic eddy heat transport. Journal of Physical Oceanography 32, 3328–3345.
Jeong, J., Hussain, F., 1995. On the identification of a vortex. Journal of Fluid Mechanics 285, 69–94.
Lagerloef, G.S.E., Mitchum, G., Lukas, R., Niiler, P., 1999. Tropical Pacific near-surface currents estimated from altimeter, wind and drifter data. Journal of Geophysical Research – Oceans 104, 23313–23326.
Le Traon, P.Y., Dibarboure, G., 1999. Mesoscale mapping capabilities from multiple altimeter missions. Journal of Atmospheric and Oceanic Technology 16, 1208–1223.
Le Traon, P.-Y., Morrow, R., 2001. Ocean currents and eddies. In: Fu, L.-L., Cazenave, A. (Eds.), Satellite Altimetry and Earth Sciences: A Handbook of Techniques and Applications. Elsevier, New York, p. 57.
Le Traon, P.-Y., Nadal, F., Ducet, N., 1998. An improved mapping method of multi-satellite altimeter data. Journal of Atmospheric and Oceanic Technology 15, 522–534.
Le Traon, P.Y., Dibaboure, G., Ducet, N., 2001. Use of a high-resolution model to analyze the mapping capabilities of multiple-altimeter missions. Journal of Atmospheric and Oceanic Technology 18, 1277–1288.
Leeuw, W.C., Post, F.H., 1995. A Statistical View on Vector Fields. Visualization in scientific Computing. Springer-Verlag.
Logerwell, E.A., Smith, P.E., 2001. Mesoscale eddies and survival of late stage Pacific sardine (*Sardinops sagax*) larvae. Fisheries Oceanography 10 (1), 13–25.
Loubere, P., 2000. Marine control of biological production in the eastern equatorial Pacific. Nature 406, 497–500.
Maharaj, A.M., Cipollini, P., Holbrook, N.J., 2005. Observed variability of the South Pacific westward sea level anomaly signal in the presence of bottom topography. Geophysical Research Letters 32 (4). doi:10.1029/2004GL020966.
McGillicuddy, D.J., Robinson, A.R., Siegel, D.A., Jannasch, H.W., Johnson, R., Dickey, T.D., McNeil, J.D., Michaels, A.F., Knap, A.H., 1998. New evidence for the impact of mesoscale eddies on biogeochemical cycling in the Sargasso Sea. Nature 394, 263–266.
McPhaden, M.J., 2006. ENSO as an integrated concept in Earth science. Science 314, 1740–1745.
Mitchell, T.P., Wallace, J.M., 1992. The annual cycle in equatorial convection and sea-surface temperature. Journal of Climate 5, 1140–1156.
Morrow, R., Donguy, J.-R., Chaigneau, A., Rintoul, S.R., 2004a. Cold-core anomalies at the Subantarctic Front, South of Tasmania. Deep-Sea Research I 51, 1417–1440.
Morrow, R., Birol, F., Griffin, D., Sudre, J., 2004b. Divergent pathways of cyclonic and anti-cyclonic ocean eddies. Geophysical Research Letters 31, L24311. doi:10.1029/2004GL020974.
Nielsen, J.W., Dole, R.M., 1992. A survey of extratropical cyclone characteristics during GALE. Monthly Weather Review 120, 1156–1167.
Okubo, A., 1970. Horizontal dispersion of floatable particles in the vicinity of velocity singularities such as convergences. Deep-Sea Research 17, 445–454.
Pascual, A., Faugère, Y., Larnicol, G., Le Traon, P.Y., 2006. Improved description of the ocean mesoscale variability by combining four satellite altimeters. Geophysical Research Letters 33, L02611. doi:10.1029/2005GL024633.
Penven, P., Echevin, V., Pasapera, J., Colas, F., Tam, J., 2005. Average circulation, seasonal cycle, and mesoscale dynamics of the Peru Current System: a modeling approach. Journal of Geophysical Research – Oceans 110, C10021. doi:10.1029/2005JC002945.
Pizarro, O., Shaffer, G., Dewitte, B., Ramos, M., 2002. Dynamics of seasonal and interannual variability of the Peru–Chile Undercurrent. Geophysical Research Letters 29 (12), 1581. doi:10.1029/2002GL014790.
Qiu, B., Chen, S., 2005. Eddy-induced heat transport in the subtropical North Pacific from Argo, TMI and altimetry measurements. Journal of Physical Oceanography 35, 458–473.
Rio, M.-H., Hernandez, F., 2004. A Mean Dynamic Topography computed over the world ocean fromaltimetry, in-situmeasurements and a geoid model. Journal of Geophysical Research – Oceans 109 (12).
Rio, M.-H., Poulain, P.-M., Pascual, A., Mauri, E., Larnicol, G., Santoleri, R., 2007. A mean dynamic topography of the Mediterranean Sea computed from altimetric data, in-situ measurements and a general circulation model. Journal of Marine Systems 65, 484–508.
Robinson, S.K., 1991. Coherent Motions in the Turbulent Boundary Layer. Annual Review of Fluid Mechanics 23, 601–639.
Roemmich, D., Gilson, J., 2001. Eddy transport of heat and thermocline waters in the North Pacific: a key to interannual/decadal climate variability? Journal of Physical Oceanography 31, 675–687.
Sadarjoen, A., 1999. Extraction and visualization of geometries in fluid flow fields. Ph.D. Thesis, Delft University, Germany, unpulished, 145 pp.
Sadarjoen, A., Post, F.H., 2000. Detection, quantification, and tracking of vortices using streamline geometry. Visualization and Computer Graphics 24, 333–341.
Sadarjoen, A., Post, F. H., Ma, B., Banks, D. C., Pagendarm, H.-G., 1998. Selective visualization of vortices in hydrodynamics flows. In: Proceedings of Visualization'98, Research Triangle Park, NC, pp. 419–422.
Sasai, Y., Ishida, A., Sasaki, H., Kawahara, S., Uehara, H., Yamanaka, Y., 2006. A global eddy-resolving coupled physical-biological model: physical influences on a marine ecosystem in the North Pacific. Simulation 82 (7), 467–474.
Segond, M., 2006. Algorithmes bio-mimétiques pour la reconnaissance de formes et l'apprentissage. Ph.D. thesis, Université de Litoral-côte d'opale, France, 138 pp., unpublished.
Shaffer, G., Pizarro, O., Djurfeldt, L., Salinas, S., Ruttlant, J., 1997. Circulation and low-frequency variability near the Chilean coast: Remotely forced fluctuations during the 1991–1992 El Niño. Journal of Physical Oceanography 27, 217–235.
Siegel, D., McGillicuddy, D., Fields, E., 1999. Mesoscale eddies, satellite altimetry, and new production in the Sargasso Sea. Journal of Geophysical Research – Oceans 104 (C6). doi:10.1029/1999JC900051.
Spear, L.B., Balance, L.T., Ainley, D.G., 2001. Response of seabirds to thermal boundaries in the tropical Pacific: the thermocline versus the Equatorial Front. Marine Ecology Progress Series 219, 275–289.
Stammer, D., 1997. Global characteristics of ocean variability estimated from regional TOPEX/POSEIDON altimeter measurements. Journal of Physical Oceanography 27, 1743–1769.
Stammer, D., 1998. On eddy characteristics, eddy transports, and mean flow properties. Journal of Physical Oceanography 28, 727–739.
Stammer, D., Wunsch, C., 1999. Temporal changes in eddy energy of the oceans. Deep-Sea Research II 46, 77–108.
Stammer, D., Wunsch, C., Ueyoshi, K., 2006. Temporal changes in ocean heat transports. Journal of Physical Oceanography 36, 543–550.
Strub, P.T., Mesias, J.M., Montecino, V., Rutllant, J., Salinas, S., 1998. Coastal ocean circulation off western South America. In: Robinson, A.R., Brink, K.H. (Eds.), The Sea, vol. 11. John Wiley, Hoboken, N. J, pp. 273–313.
Takahashi, K., 2005. The annual cycle of heat content in the Peru-Current region. Journal of Climate 18, 4937–4954.
Thomas, A., 1999. Seasonal distributions of satellite-measured phytoplankton pigment concentration along the Chilean coast. Journal of Geophysical Research – Oceans 104 (C11). doi:10.1029/1999JC900171.
Thomas, A.C., Huang, F., Strub, P.T., James, C., 1994. Comparison of the seasonal and interannual variability of phytoplankton pigment concentrations in the Peru and California Current systems. Journal of Geophysical Research 99 (C4). doi:10.1029/93JC02146.
Vázquez, L., García, W., 2001. Condiciones oceanográficas del mar peruano durante el verano 2000. Informe del Instituto del Mar del Perú 159, 65–72.
Wang, X.L., Swail, V.R., Zwiers, F.W., 2006. Climatology and changes of extratropical cyclone activity: comparison of ERA-40 with NCEP–NCAR reanalysis for 1958–2001. Journal of Climate 19, 3145–3166.
Weiss, J., 1991. The dynamics of enstrophy transfer in two-dimensional hydrodynamics. Physica D 48, 273–294.
Wunsch, C., 1999. Where do ocean eddy heat fluxes matter? Journal of Geophysical Research – Oceans 104, 13235–13249.
Zamudio, L., Leonardi, A.P., Meyers, S.D., O'Bryen, J.J., 2001. ENSO and eddies on the southwest coast of Mexico. Geophysical Research Letters 28, 13–16.
Zhang, X., Walsh, J.E., Zhang, J., Bhatt, U.S., Ikeda, M., 2004. Climatology and interannual variability of Arctic cyclone activity: 1948–2002. Journal of Climate 17, 2300–2317.